Article

Heterodimensional superlattice with in-plane anomalous Hall effect

https://doi.org/10.1038/s41586-022-05031-2

Received: 17 March 2021

Accepted: 28 June 2022

Published online: 31 August 2022

Check for updates

Jiadong Zhou[1,16]✉, Wenjie Zhang[2,3,16], Yung-Chang Lin[4,16], Jin Cao[1,16], Yao Zhou[5,6], Wei Jiang[1], Huifang Du[1], Bijun Tang[5], Jia Shi[7], Bingyan Jiang[2], Xun Cao[5], Bo Lin[5], Qundong Fu[5], Chao Zhu[5], Wei Guo[1], Yizhong Huang[5], Yuan Yao[8], Stuart S. P. Parkin[3], Jianhui Zhou[9], Yanfeng Gao[10], Yeliang Wang[11], Yanglong Hou[12], Yugui Yao[1]✉, Kazu Suenaga[5]✉, Xiaosong Wu[2,13]✉ & Zheng Liu[5,14,15]✉

Superlattices—a periodic stacking of two-dimensional layers of two or more materials—provide a versatile scheme for engineering materials with tailored properties[1,2]. Here we report an intrinsic heterodimensional superlattice consisting of alternating layers of two-dimensional vanadium disulfide (VS_2) and a one-dimensional vanadium sulfide (VS) chain array, deposited directly by chemical vapour deposition. This unique superlattice features an unconventional 1T stacking with a monoclinic unit cell of VS_2/VS layers identified by scanning transmission electron microscopy. An unexpected Hall effect, persisting up to 380 kelvin, is observed when the magnetic field is in-plane, a condition under which the Hall effect usually vanishes. The observation of this effect is supported by theoretical calculations, and can be attributed to an unconventional anomalous Hall effect owing to an out-of-plane Berry curvature induced by an in-plane magnetic field, which is related to the one-dimensional VS chain. Our work expands the conventional understanding of superlattices and will stimulate the synthesis of more extraordinary superstructures.

Superlattices have drawn intensive attention owing to their intriguing electronic, optical and magnetic properties that do not exist in intrinsic materials[1–5]. In general, traditional superlattices have been formed among materials with the same dimension (such as three-dimensional (3D)–3D, two-dimensional (2D)–2D and one-dimensional (1D)–1D superlattices)[2,6–8]. Recently, breakthroughs in 2D materials have enriched the superlattice families, including van der Waals heterostructures, moiré periodic patterns and randomly intercalated compounds[9,10]. For instance, various typical superlattices—such as the moiré superlattices of hexagonal boron nitride/graphene[11] and twisted graphene[12], intermixing of $((GeTe)_x/(Sb_2Te_3)_y)_n$ (ref. [13]) and organic molecular (cetyltrimethyl ammonium bromide) intercalated black phosphorus[14], and the molecule molybdenum disulfide—have been achieved[15]. In addition, intercalated compounds including niobium-based[16] and vanadium-based[17] superlattices and the intrinsic 2D superlattice $MnBi_2Te_4$ (ref. [18]) have been reported. These superlattices possess the potential superconductivity[19] and ferromagnetism[20] required for applications in quantum spintronic devices[21–23]. However, these superlattices were mostly obtained by epitaxial growth or assembled by stacking 2D materials through different methods[6,24–27]. Furthermore, in terms of the structures and dimensions, the reported superlattices are 3D–3D, 2D–2D and 1D–1D superlattices[6,16,17]. The realization of an intrinsic heterodimensional superlattice formed between an intrinsic 2D (or 3D) material and a 1D material is still a big challenge in experiments[28].

Here we report a heterodimensional intrinsic superlattice structure in a vanadium (V)-based 2D superlattice grown directly by a one-step chemical vapour deposition (CVD) method. This superlattice is a periodic structure of a 2D vanadium disulfide (VS_2) layer and a 1D vanadium sulfide (VS) chain array, belonging to the $C2/m$ space group with monoclinic symmetry. Such a structure has not been expected in metallurgy. Owing to the existence of the 2D VS_2 and the 1D VS array, the superlattice (VS_2–VS) shows an intriguing room-temperature in-plane anomalous Hall effect. The magnetic-field angular dependence of this effect indicates that only the magnetization along a particular crystalline direction contributes. The strong anisotropy stems from the 1D nature of the unique VS chain in the superlattice. Our work opens an avenue to explore heterodimensional superlattices with excellent physical properties.

[1]Centre for Quantum Physics, Key Laboratory of Advanced Optoelectronic Quantum Architecture and Measurement (MOE), School of Physics, Beijing Institute of Technology, Beijing, China. [2]State Key Laboratory for Artificial Microstructure and Mesoscopic Physics, Frontiers Science Center for Nano-optoelectronics, and Collaborative Innovation Center of Quantum Matter, Peking University, Beijing, China. [3]Max Planck Institute of Microstructure Physics, Halle, Germany. [4]The Institute of Scientific and Industrial Research, Osaka University, Osaka, Japan. [5]School of Materials Science and Engineering, Nanyang Technological University, Singapore, Singapore. [6]Advanced Research Institute of Multidisciplinary Science, and School of Chemistry and Chemical Engineering, Beijing Institute of Technology, Beijing, China. [7]Department of Chemistry, National University of Singapore, Singapore, Singapore. [8]Institute of Physics, Chinese Academy of Sciences, Beijing, China. [9]Anhui Key Laboratory of Condensed Matter Physics at Extreme Conditions, High Magnetic Field Laboratory, HFIPS, Anhui, Chinese Academy of Sciences, Hefei, China. [10]School of Materials Science and Engineering, Shanghai University, Shanghai, China. [11]School of Integrated Circuits and Electronics, Beijing Institute of Technology, Beijing, China. [12]Beijing Key Laboratory for Magnetoelectric Materials and Devices, Beijing Innovation Center for Engineering Science and Advanced Technology, School of Materials Science and Engineering, Peking University, Beijing, China. [13]Shenzhen Institute for Quantum Science and Engineering, Southern University of Science and Technology, Shenzhen, China. [14]CINTRA CNRS/NTU/THALES, UMI 3288, Singapore, Singapore. [15]School of Electrical and Electronic Engineering, Nanyang Technological University, Singapore, Singapore. [16]These authors contributed equally: Jiadong Zhou, Wenjie Zhang, Yung-Chang Lin, Jin Cao. ✉e-mail: jdzhou@bit.edu.cn; ygyao@bit.edu.cn; suenaga-kazu@sanken.osaka-u.ac.jp; xswu@pku.edu.cn; z.liu@ntu.edu.sg

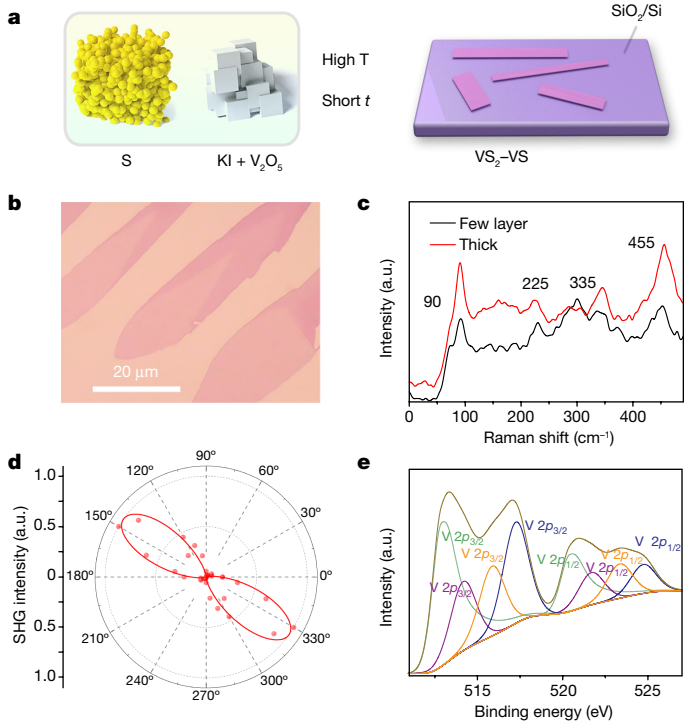

Fig. 1 | Growth process and optical images of the VS_2–VS superlattice. **a**, Growth process of VS_2–VS. At a high temperature (*T*) with a short growth time (*t*), a VS_2–VS superlattice can be obtained. **b**, Optical image of VS_2–VS superlattice flakes. **c**, Raman spectra of the VS_2–VS superlattice with different thicknesses. **d**, Azimuthal-angle dependence of the SHG intensity in VS_2–VS, illustrating its anisotropic property. The red dots and red line are the measurement data and fitted SHG curve of the VS_2–VS superlattice, respectively. **e**, XPS spectra of V 2*p* in the VS_2–VS superlattice. The V $2p_{1/2}$ and V $2p_{3/2}$ located at 523 eV and 516 eV (orange curve) correspond to the V^{4+} in VS_2. The V $2p_{1/2}$ and V $2p_{3/2}$ located at 521 eV and 514.5 eV are attributed to the V^{2+} in VS. The V $2p_{1/2}$ and V $2p_{3/2}$ located at 520.3 eV and 513 eV highlighted by green curve are induced by the V element that has not reacted with S. The V $2p_{1/2}$ and V $2p_{3/2}$ located at high energy are attributed to oxidization of the superlattice, and have also been observed in the XPS spectra of S.

Synthesis of VS_2–VS superlattice

It is noted that VS_2 and V_5S_8 can be easily obtained by the CVD method[17,29–31]. In our experiment, a VS_2–VS superlattice was successfully achieved by controlling the growth conditions. Herein, a molten-salt CVD method was used to synthesize the V-based superlattices[29]. The corresponding set-up is shown in Supplementary Fig. 1. The growth method is depicted in Fig. 1a. The preparation of VS_2, V_5S_8 and the VS_2–VS superlattice is discussed in Supplementary Section I (Supplementary Figs. 1 and 2, and Supplementary Table 1). By controlling the temperature of sulfur, at a high growth temperature with a short growth time (less than 2 min), a VS_2–VS superlattice was achieved. At a low growth temperature (lower than 730 °C) with a long growth time (more than 3 min), VS_2 flakes were obtained (as shown in Supplementary Fig. 3). Figure 1b shows an optical image of the VS_2–VS superlattice, which was synthesized with a precursor ratio of V_2O_5:potassium iodide (KI) greater than 5:1. It can be clearly seen in Supplementary Fig. 4 that the VS_2–VS superlattice has a needle-like shape. At a low precursor ratio of 2:1, the superlattice array was obtained (Supplementary Fig. 5). This is attributed to the vapour–liquid–solid growth mechanism[32], which is discussed in Supplementary Fig. 2. The yield and the stability of the superlattice are discussed in Supplementary Figs. 4–7. Atomic force microscopy measurements are detailed in Supplementary Fig. 8. Raman spectroscopy was performed to determine the vibrational properties of the VS_2–VS superlattice (Supplementary Fig. 6). Four main peaks located at around 90 cm^{-1}, 225 cm^{-1}, 345 cm^{-1} and 455 cm^{-1} were observed, as shown in Fig. 1c, which are completely different from the Raman spectra of VS_2 (ref. [33]). The Raman modes of the superlattices were identified by density functional theory (DFT) calculations, as shown in Supplementary Fig. 9 and Supplementary Table 2. We further measured the optical second-harmonic generation (SHG) from thick samples and a wavelength of about 990 nm was selected as the excitation wavelength. An SHG signal clearly appears at 495 nm (Supplementary Fig. 10). The dependence of the SHG intensity on the azimuthal angle is shown in Fig. 1d (see more discussion in Supplementary Information). To further illustrate the valence state of V in the superlattice, X-ray photoelectron spectroscopy (XPS) was conducted and the results are presented in Fig. 1e. We can clearly see that both V^{4+} and V^{2+} co-exist in the superlattice, which suggests the formation of V–S bonds. The V 2*p* peaks located at 525 eV and 517 eV are induced by oxidation of the samples. The corresponding XPS spectra for sulfur (S) are shown in Supplementary Fig. 11.

Microstructure characterization

To determine the atomic structure of as-synthesized superlattices, annular dark-field scanning transmission electron microscopy (ADF-STEM) and cross-section transmission electron microscopy (TEM) were performed. The grown material is a superlattice consisting of a periodic structure of 2D VS_2 and a 1D VS chain array. Figure 2a,b shows the unit cell and the stacking structure of the VS_2–VS superlattice with the atomic model from the top view and the side view, respectively. The VS_2 monolayers exhibit a 1T phase where the V and S atoms are arranged in octahedral coordination. The VS chains are a 1D infinite array structure, stacking between the VS_2 layers, forming a large (1 × 3) surface unit cell in which the V atoms are trigonal pyramid coordinated by S atoms. The VS_2–VS superlattice belongs to the monoclinic crystal system with a *C*2/*m* space group, where the unit cell (green dashed rhombus in Fig. 2b) consists of lattice parameters $a = 9.69$ Å, $b = 3.23$ Å, $c = 8.60$ Å, $\alpha = 90°$, $\beta = 101°$ and $\gamma = 60°$. It is noted that the stacking order of the VS_2 layers is not conventional 1T stacking but a 3R (rhombohedral) stacking (indicated by the black dashed box in Fig. 2b) with the VS chain array intercalated. Figure 2c shows an ADF image of the VS_2–VS superlattice cross-section taken using 60-kV aberration-corrected STEM. The magnified ADF cross-section image from the dashed rectangle in Fig. 2c is shown in Fig. 2d. The special stacking order matches the atomic model shown in Fig. 2a,b well. Some weak atomic contrasts appear in the interval of VS chains, which should originate from part of the displaced VS chains along the longitudinal axis (Supplementary Fig. 12).

Figure 3a shows a coloured low-magnification ADF image of the superlattice from the top view, and the number of layers (labelled with circled numbers) can be easily distinguished by the contrast. Figure 3b shows an ADF image from the thinnest area. We found that the VS array layer is not stable when it is exposed at the surface (see also Figs. 2c and 3e). As a result, the thinnest stable structure is one VS array layer sandwiched between two layers of VS_2. The fast Fourier transform (FFT) image shown in Fig. 3b reveals structural information on the superlattice, which consists of a (1 × 1) hexagonal pattern and (1 × 1/3) satellite spots for the VS_2 layers and the VS array layers, respectively. Furthermore, Fig. 3c,d (left) shows magnified ADF images of the thinnest and second-thinnest VS_2–VS superlattice, respectively. The corresponding simulation results (Fig. 3c,d, right) show excellent fit to the experimental measurements. More details about the structure of the VS_2–VS superlattice are shown in Supplementary Fig. 13.

We further performed electron energy loss spectroscopy (EELS) to investigate the charged state of the vanadium in the VS_2 and VS chains. Figure 3e shows an ADF image of the thinnest superlattice as $2VS_2 + 1VS$. In the top-right corner, one layer of VS_2 and VS chains were damaged by the e-beam and left a monolayer of VS_2 exposed. We performed an

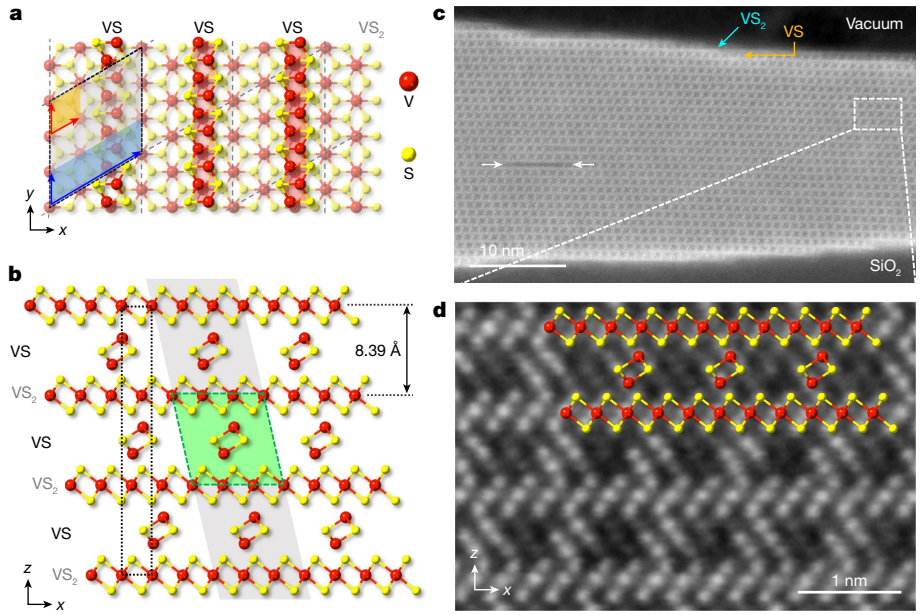

Fig. 2 | Atomic structure of the VS_2–VS superlattice. a, Top-view atomic model of the stacking structure of the VS_2–VS superlattice. The red and yellow balls represent V and S atoms, respectively. The red arrows indicate the (1 × 1) unit cell (orange colour) of the VS_2 lattice. The blue arrows indicate the (1 × 3) unit cell (cyan colour) of the VS chain array. The red bands highlight the 1D VS arrays. **b**, Side-view atomic model of the VS_2–VS superlattice. The black dashed box indicates the 3R stacking structure of 1T-VS_2. The VS_2–VS superlattice can be expressed by a smaller unit cell (green dashed rhombus) with lattice parameters of $a = 9.69$ Å, $b = 3.23$ Å, $c = 8.60$ Å, $\alpha = 90°$, $\beta = 101°$ and $\gamma = 60°$. The grey band indicates the periodicity of the superlattice unit cell along the c axis. **c**, Cross-section ADF image of the VS_2–VS superlattice cut by focused ion beam. The surface is terminated in a VS_2 layer. A local deficiency in the 1D VS chains is indicated by the white arrows. **d**, The magnified ADF image from the white rectangle in **c** that agrees with the overlaid atomic model structure.

EELS line scan along the green line in Fig. 3e across seven VS chains. Figure 3f shows the 2D spectrum image with energy on the x axis and scan distance on the y axis. The cyan arrows point to the vanadium L-edges collected from pure VS_2, and the orange arrows point to the spectra that contain extra EELS signals from the VS chains. Figure 3g shows the EELS spectra of VS_2 + VS and VS_2, which are combined spectra from the seven orange arrows and seven cyan arrows in Fig. 3f, respectively. The cyan spectrum represents the V^{4+} of VS_2, and the orange spectrum contains an extra signal from V^{2+} of VS with a redshift of the L-edge and an increase in the L_2 peak. It is noted that no potassium and iodine signals were detected from the EDS and EELS spectrum of the VS_2–VS layer (Supplementary Fig. 14). The calculated Helmholtz free energies of the VS_2–VS superlattices and VS_2 are shown in Supplementary Fig. 15, demonstrating that the VS_2–VS superlattices are stable and naturally exist.

Properties of the VS_2–VS superlattice

Owing to the novel structure of the van der Waals superlattice formed by the layered VS_2 and VS array, the superlattice shows a striking property, that is, an unexpected Hall effect when a magnetic field is in the plane of the electric current and the Hall field. Figure 4a shows the field dependence of the Hall resistivity ρ_{xy} at 150 K for fields along three coordinate axes, x, y and z, defined in Fig. 2. The current is in the y direction, and the transverse voltage along the x direction is measured. The z axis is perpendicular to the substrate. When $B||z$, the out-of-plane Hall effect (OPHE) is measured. When B is in the x–y plane, the Hall effect usually vanishes because of the absence of the Lorentz force contribution, as is observed when $B||y$. The vanishing ρ_{xy} indicates a good alignment accuracy in our experimental set-up. However, when $B||x$, there is a marked Hall effect that is even larger than the OPHE, which immediately rules out the possibility of a perpendicular field contribution owing to misalignment of the sample. Herein, we call this unconventional Hall effect the in-plane Hall effect (IPHE). It is worth pointing out that the IPHE should not be confused with the planar Hall effect, which is essentially an anisotropic magnetoresistance[34–36]. The IPHE is a true dissipationless Hall effect, which is independent of the direction of the current, that is, it persists even when the current is parallel to the magnetic field (Supplementary Fig. 16). As the ordinary Hall cannot play a role under the current geometry, we believe that the IPHE is a type of anomalous Hall effect (AHE) associated with spin–orbit coupling.

Unlike typical nonlinear AHE in ferromagnets, our IPHE is linear in field at all measurement temperatures, which excludes any ferromagnetic order. Among all known vanadium sulfite compounds, only V_5S_8 and V_3S_4 exhibit an antiferromagnetic order below 32 K and 9 K, respectively[9,37]. The phase transition is manifested as a kink in the temperature-dependent resistivity[38]. However, the resistivity of our superlattice remains smooth up to 380 K (Supplementary Fig. 17), implying an absence of magnetic order. This is further supported by the lack of a spin-flop transition up to 9 T, as indicated by the linear magnetoresistance and Hall resistivity (Fig. 4a and Supplementary Fig. 18). In contrast, such a transition occurs at 3.5 T in V_5S_8, owing to a relatively small magneto-crystalline anisotropy[30]. A comparison between the VS_2–VS superlattice and V_5S_8 is provided in Supplementary Fig. 17. In addition, magneto-optical Kerr effect measurements also show no signature of magnetic order (Supplementary Fig. 19).

The observed IPHE is robust, persisting up to 380 K, the highest temperature of our measurement apparatus. The magnitude decreases with increasing temperature, as shown in Fig. 4b. Surprisingly, the Hall coefficient of the IPHE at room temperature, 0.44×10^{-3} cm^3 C^{-1}, is still larger than that of the OPHE (Supplementary Figs. 20–22). The in-plane Hall conductivity is plotted as a function of temperature in Fig. 4c. Interestingly, it follows an exponential decay with temperature in the whole temperature range, which yields a gap $\Delta \approx 8$ meV (Supplementary Fig. 23). The intrinsic AHE is determined by the Berry curvature of the Bloch bands, which is inversely proportional to the square of the bandgap within the prototypical model for 2D massive Dirac fermions[39]. Consequently, the AHE is strongly enhanced when two bands

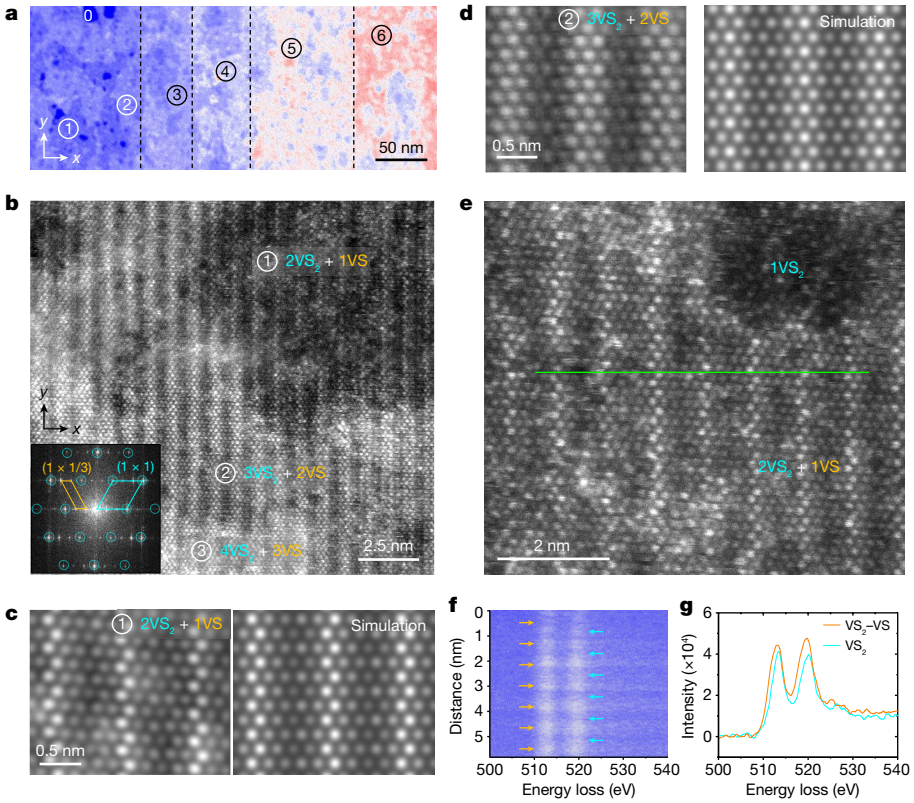

Fig. 3 | Detailed analyses of the VS_2–VS superlattice. a, A coloured low-magnification ADF image of the superlattice. The darkest contrast region marked with 0 is the vacuum. The different sets of superlattice layers are marked by circled numbers. **b**, An atomic-resolution ADF image of the superlattice at the thinnest region. **c**,**d**, Magnified ADF image and corresponding simulation image of the thinnest and second-thinnest superlattices as $2VS_2 + 1VS$ (**c**) and $3VS_2 + 2VS$ (**d**). **e**, An ADF image of the $2VS_2 + 1VS$ region with an area exposing monolayer VS_2. **f**, EELS 2D spectrum image taken from a line scan along the green line in **e**. Orange and cyan arrows point to the positions of the VS_2 + VS and VS_2 regions, respectively. **g**, EELS spectra of the vanadium L-edge of the VS_2 + VS region (orange spectrum) and the VS_2 region (cyan spectrum).

are close, known as hotspots. The obtained small gap is consistent with the observed substantial IPHE. This picture is supported by the distributions of Berry curvature in the Brillouin zone from the DFT calculations (Supplementary Fig. 29).

The link between the particular superlattice structure and the unconventional property can be qualitatively uncovered to some extent by following the symmetry arguments in refs. [40,41] (further details can be found in Supplementary Sections II and VII). Our superlattice has a $C2/m$ space group, which has a glide mirror symmetry $\widetilde{M}_y = \left\{M_y \middle| \frac{\mathbf{a}}{2}, \frac{\mathbf{b}}{2}, 0\right\}$ (Fig. 2), forcing the IPHE to vanish. However, an in-plane magnetization $\mathbf{m}_{\parallel}$ breaks the mirror symmetry and the Hall effect is allowed, except when $\mathbf{m}_{\parallel}$ is parallel to the y axis. $\widetilde{M}_y$ survives, resulting in a zero Hall effect, which is confirmed by calculation (Supplementary Fig. 30) and in excellent agreement with the experimental results. The symmetry analysis also provides a guideline for searching for the IPHE. For example, if there are two perpendicular mirror planes that are also perpendicular to the Hall plane, the IPHE is forbidden.

It is well understood that the Berry curvature acts on electrons like a magnetic field in momentum space and gives rise to the intrinsic AHE. Although the intrinsic anomalous Hall conductivity (AHC) is usually aligned with magnetization, it is not a requirement. In fact, it has been predicted that an in-plane magnetization can produce the quantum version of the AHE[40,42]. Our superlattice presents a rare case of an out-of-plane Berry curvature generated by an in-plane field. To further reveal the origin of the IPHE, we performed DFT calculations of the band structure involving the spin–orbit coupling and a magnetic field (see more details of calculation in Supplementary Section VIII), which splits the energy bands (Supplementary Fig. 29). We found that the spin–orbit coupling and magnetic field combine to induce an inhomogeneous distribution of Berry curvature of the energy bands, which is mainly concentrated around the regions with small bandgaps such as the G point in the Brillouin zone (Supplementary Fig. 30), in line with our aforementioned qualitative analysis of the Berry curvature. The calculated field-dependent intrinsic AHC (Supplementary Fig. 30) exhibits several key features consistent with experiments. (We clarify the possibility of the IPHE owing to the Lorentz force with an anisotropic Fermi surface (Supplementary Fig. 31).) First, the AHC vanishes when the magnetic field is along the y direction, but is finite otherwise. Second, the moderate magnetic field would enhance the magnetization and hence increase the AHC linearly, which agrees with the experimental linear magnetic-field dependence of the AHC.

We then map out the magnetic-field angular dependence of the Hall effect, as shown in Fig. 4d–f. As the field is rotated in the z–y plane, the Hall resistivity follows a sine function, consistent with a conventional Hall effect due to the out-of-plane field. In the case of the field being rotated in the x–y plane, the Hall resistivity maximizes when $B||x$, whereas it vanishes when $B||y$, again following a simple sine function. When the field is rotated in the z–x plane, the measured data are a sine function with a phase shift, which can be faithfully decomposed into the IPHE and the OPHE without any adjusting parameter (see the illustration in Supplementary Figs. 24 and 25). The fact that the angular dependence can be well described by simple trigonometric functions indicates that the IPHE is solely proportional to the projection of the field on the x axis. This result, though seemingly trivial, implies a highly unusual spin texture, which apparently results from the peculiar 1D VS chain of the superlattice, as it breaks the three-fold rotational symmetry of VS_2.

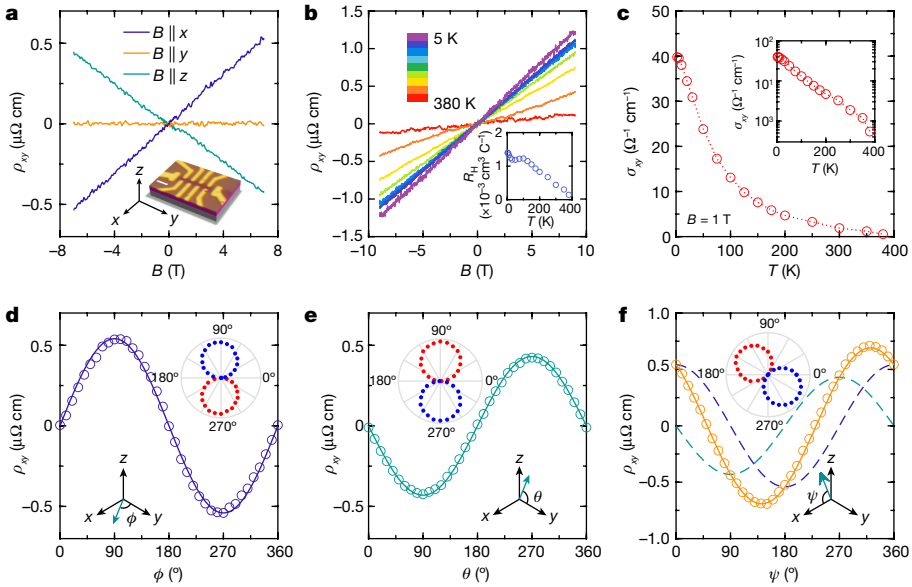

Fig. 4 | Transport measurements of the VS_2–VS superlattice. a, Hall resistivity under a magnetic field along different directions at $T = 150$ K. As the magnetoresistance is negligible at this temperature (Supplementary Fig. 18), only a constant value needs to be subtracted from the raw data to obtain the Hall resistivity. The in-plane Hall effect ($B||x$) is even larger than the out-of-plane one ($B||z$). The inset is an illustration of a typical sample. Scale bar, 2 μm. The current is along the y direction. **b**, IPHE at different temperatures. The inset is the temperature dependence of the Hall coefficient. **c**, In-plane Hall conductivity versus temperature. The inset shows the Hall conductivity calculated from the resistivity and the Hall resistivity at $B = 1$ T, plotted on a semi-log scale. **d**–**f**, Angular dependence of Hall resistivity at $B = 7$ T for a field in the x–y (**d**), y–z (**e**) and x–z (**f**) planes. Solid lines in **d** and **e** represent fits to sine functions. The data in **f** can be decomposed as the sum (solid orange line) of the in-plane component (cosine, dashed blue line) and the out-of-plane component (sine, dashed green line). The insets in **d** and **f** show the angular dependence in a polar diagram. The red and blue colours represent the positive and the negative signs of the Hall resistivity, respectively, and the radius represents the absolute value. The data in **d**–**f** are measured at 150 K. The data in **a** and **d**–**f** are from one sample and the data in **b** and **c** are from another sample.

Conclusion

We have synthesized a vertically stacked VS_2–VS superlattice using the CVD method. The STEM and cross-section TEM results clearly revealed the atomic structure of the VS_2–VS superlattice, which has not been obtained in V-based materials. The in-plane AHE at room temperature was first observed in the superlattice. The magnetic-field angular dependence reveals an unexpected in-plane anisotropy, resulting from the 1D VS chain. Our results open an avenue to synthesize superlattices and uncover novel physical properties.

Online content

Any methods, additional references, Nature Research reporting summaries, source data, extended data, supplementary information, acknowledgements, peer review information; details of author contributions and competing interests; and statements of data and code availability are available at https://doi.org/10.1038/s41586-022-05031-2.

1. Novoselov, K. S., Mishchenko, A., Carvalho, A. & Castro Neto, A. H. 2D materials and van der Waals heterostructures. *Science* **353**, aac9439 (2016).
2. Esaki, L. & Chang, L. L. New transport phenomenon in a semiconductor "superlattice". *Phys. Rev. Lett.* **33**, 495–498 (1974).
3. Liu, Y. et al. Van der Waals heterostructures and devices. *Nat. Rev. Mater.* **1**, 16042 (2016).
4. Björk, M. T. et al. One-dimensional steeplechase for electrons realized. *Nano Lett.* **2**, 87–89 (2002).
5. Dumestre, F., Chaudret, B., Amiens, C., Renaud, P. & Fejes, P. Superlattices of iron nanocubes synthesized from $Fe[N(SiMe_3)_2]_2$. *Science* **303**, 821–823 (2004).
6. Ryu, Y. K., Frisenda, R. & Castellanos-Gomez, A. Superlattices based on van der Waals 2D materials. *Chem. Commun.* **55**, 11498–11510 (2019).
7. Hu, M. & Poulikakos, D. Si/Ge superlattice nanowires with ultralow thermal conductivity. *Nano Lett.* **12**, 5487–5494 (2012).
8. Davies, R. A., Kelly, M. J., Kerr, T. M., Hetherington, C. J. D. & Humphreys, C. J. Geometric and electronic structure of a semiconductor superlattice. *Nature* **317**, 418–419 (1985).
9. Silbernagel, B. G., Levy, R. B. & Gamble, F. R. Magnetic properties of V_5S_8: an NMR study. *Phys. Rev. B* **11**, 4563–4570 (1975).
10. Jariwala, D., Marks, T. J. & Hersam, M. C. Mixed-dimensional van der Waals heterostructures. *Nat. Mater.* **16**, 170–181 (2017).
11. Yankowitz, M. et al. Emergence of superlattice Dirac points in graphene on hexagonal boron nitride. *Nat. Phys.* **8**, 382–386 (2012).
12. Cao, Y. et al. Unconventional superconductivity in magic-angle graphene superlattices. *Nature* **556**, 43–50 (2018).
13. Li, X.-B., Chen, N.-K., Wang, X.-P. & Sun, H.-B. Phase-change superlattice materials toward low power consumption and high density data storage: microscopic picture, working principles, and optimization. *Adv. Funct. Mater.* **28**, 1803380 (2018).
14. Wang, C. et al. Monolayer atomic crystal molecular superlattices. *Nature* **555**, 231–236 (2018).
15. Zhong, Y. et al. Wafer-scale synthesis of monolayer two-dimensional porphyrin polymers for hybrid superlattices. *Science* **366**, 1379–1384 (2019).
16. Yang, J. et al. Ultrahigh-current-density niobium disulfide catalysts for hydrogen evolution. *Nat. Mater.* **18**, 1309–1314 (2019).
17. Ji, Q. et al. Metallic vanadium disulfide nanosheets as a platform material for multifunctional electrode applications. *Nano Lett.* **17**, 4908–4916 (2017).
18. Deng, Y. et al. Quantum anomalous Hall effect in intrinsic magnetic topological insulator $MnBi_2Te_4$. *Science* **367**, 895–900 (2020).
19. Mitchson, G. et al. Structural changes in 2D BiSe bilayers as n increases in $(BiSe)_{1+\delta}(NbSe_2)_n$ ($n = 1$–4) heterostructures. *ACS Nano* **10**, 9489–9499 (2016).
20. Li, Z. et al. Molecule-confined engineering toward superconductivity and ferromagnetism in two-dimensional superlattice. *J. Am. Chem. Soc.* **139**, 16398–16404 (2017).
21. Georgiou, T. et al. Vertical field-effect transistor based on graphene-WS_2 heterostructures for flexible and transparent electronics. *Nat. Nanotechnol.* **8**, 100–103 (2013).
22. Zhong, D. et al. Van der Waals engineering of ferromagnetic semiconductor heterostructures for spin and valleytronics. *Sci. Adv.* **3**, e1603113 (2017).
23. Hou, Y., Kim, J. & Wu, R. Magnetizing topological surface states of Bi_2Se_3 with a CrI_3 monolayer. *Sci. Adv.* **5**, eaaw1874 (2019).
24. Geim, A. K. & Grigorieva, I. V. Van der Waals heterostructures. *Nature* **499**, 419–425 (2013).
25. Haigh, S. J. et al. Cross-sectional imaging of individual layers and buried interfaces of graphene-based heterostructures and superlattices. *Nat. Mater.* **11**, 764–767 (2012).
26. Chang, L. L. & Esaki, L. Semiconductor superlattices by MBE and their characterization. *Prog. Cryst. Growth Charact.* **2**, 3–14 (1979).
27. Yao, J. et al. Optical transmission enhancement through chemically tuned two-dimensional bismuth chalcogenide nanoplates. *Nat. Commun.* **5**, 5670 (2014).
28. Devarakonda, A. et al. Clean 2D superconductivity in a bulk van der Waals superlattice. *Science* **370**, 231–236 (2020).
29. Zhou, J. et al. A library of atomically thin metal chalcogenides. *Nature* **556**, 355–359 (2018).
30. Niu, J. et al. Anomalous Hall effect and magnetic orderings in nanothick V_5S_8. *Phys. Rev. B* **96**, 075402 (2017).

31. Hardy, W. J. et al. Thickness-dependent and magnetic-field-driven suppression of antiferromagnetic order in thin V_5S_8 single crystals. *ACS Nano* **10**, 5941–5946 (2016).
32. Li, S. et al. Vapour–liquid–solid growth of monolayer MoS_2 nanoribbons. *Nat. Mater.* **17**, 535–542 (2018).
33. Yuan, J. et al. Facile synthesis of single crystal vanadium disulfide nanosheets by chemical vapor deposition for efficient hydrogen evolution reaction. *Adv. Mater.* **27**, 5605–5609 (2015).
34. Liang, S. et al. Experimental tests of the chiral anomaly magnetoresistance in the Dirac–Weyl semimetals Na_3Bi and GdPtBi. *Phys. Rev. X* **8**, 031002 (2018).
35. Wang, Y. et al. Antisymmetric linear magnetoresistance and the planar Hall effect. *Nat. Commun* **11**, 216 (2020).
36. Jiang, B. et al. Chirality-dependent Hall effect and antisymmetric magnetoresistance in a magnetic Weyl semimetal. *Phys. Rev. Lett.* **126**, 236601 (2021).
37. De Vries, A. B. & Haas, C. Magnetic susceptibility and nuclear magnetic resonance of vanadium sulfides. *J. Phys. Chem. Solids* **34**, 651–659 (1973).
38. Nozaki, H., Ishizawa, Y., Saeki, M. & Nakahira, M. Electrical properties of V_5S_8 single crystals. *Phys. Lett. A* **54**, 29–30 (1975).
39. Xiao, D., Chang, M.-C. & Niu, Q. Berry phase effects on electronic properties. *Rev. Mod. Phys.* **82**, 1959–2007 (2010).
40. Liu, X., Hsu, H. C. & Liu, C. X. In-plane magnetization-induced quantum anomalous Hall effect. *Phys. Rev. Lett.* **111**, 086802 (2013).
41. Fang, C., Gilbert, M. J. & Bernevig, B. A. Bulk topological invariants in noninteracting point group symmetric insulators. *Phys. Rev. B* **86**, 115112 (2012).
42. Liu, Z. et al. Intrinsic quantum anomalous Hall effect with in-plane magnetization: searching rule and material prediction. *Phys. Rev. Lett.* **121**, 246401 (2018).

Methods

Sample synthesis

The superlattice was synthesized in a 1-inch-diameter (2.54 cm) quartz tube. The length of the furnace was about 36 cm. The reaction system is shown in Supplementary Fig. 1. Specifically, the alumina boat containing the precursor powder was put in the centre of the tube. The mixed powder (V_2O_5) and the salt (KI) with a ratio of 10:1 to 1:1 were used as the precursors. Two silicon dioxide (SiO_2)/silicon (Si) substrates with a 285-nm SiO_2 top layer were placed on the alumina boat face to face and the mixed powder was put between the substrates. Another alumina boat containing S powder was put in the upstream of the tube furnace at 200 °C. The distance between the S boat and the precursor boat was about 18 cm. A mixed gas of hydrogen/argon with a flux gas (10/80 standard cubic centimetres per minute (s.c.c.m.)) was used as the carrier gas. The heating rate of all reactions was 50 °C min^{-1}. The growth temperature was 780–800 °C and the growth time was 1–5 min. The temperature was cooled to room temperature naturally. All reaction materials were bought from Alfa Aesar with purity more than 99%. For synthesizing the V_5S_8, VCl_3 and S were used as precursors. An alumina boat with 0.2 g VCl_3 was placed in a quartz tube (diameter of 2.54 cm). The alumina boat with a volume of (8 cm × 0.6 cm × 1.1 cm) was located at the centre of the heating zone. A SiO_2/Si substrate was placed atop the boat with the oxide surface facing down. Sulfur was put in the upstream of the tube. Hydrogen/argon (90:10 s.c.c.m.) was used as the carrier gas. The centre of the furnace was heated to 600 °C at a rate of 50 °C min^{-1}. The growth time was about 5–10 min.

SHG

The SHG experiment was carried out with a home-built optical set-up. The SHG signal was excited by a titanium:sapphire oscillator-generated laser with a wavelength of 990 nm. The linewidth of the pulse was 140 fs and the repetition rate was 80 MHz. One 100× objective lens (numerical aperture 0.9, Nikon) was set to focus the laser spot on the sample and collect the reflected SHG signal. A 750 nm short pass filter (Semrock, FF01-750/SP-25) was used to filter out the excitation laser before the generated SHG was collected by the spectrometer (Acton, Spectra Pro 2300i).

STEM-EELS

STEM images were acquired by using a ARM200F-based ultra-high vacuum microscope equipped with a JEOL delta corrector and a cold field emission gun operating at 60 kV. The probe current was about 20 pA. The convergence semi-angle and the inner acquisition semi-angle were 37 mrad and 76 mrad, respectively. Typical ADF images were taken at 1,024 × 1,024 pixel resolution and using 38.5-μs pixel time. The EELS core loss spectra were acquired by using a Gatan Rio CMOS camera optimized for low-voltage operation. The EEL spectrum was acquired by using a line scan with an exposure time of 0.05 seconds per pixel. STEM image simulation was carried out by using MacTempas software (MacTempas Version 2.4.54).

Device fabrications

The Hall bar pattern was made by standard electron-beam lithography. 5/50 nm of palladium/gold or titanium/gold was deposited as metal contacts by electron-beam evaporation. The cross-shaped pattern was etched by SF_6 using reactive ion etching. Four-probe electrical measurements were carried out using a lock-in method in an Oxford variable temperature cryostat and a commercial Physical Property Measurement System (manufactured by Quantum Design).

Data availability

Source data are provided with this paper.

Acknowledgements The work was supported by: the National Key R&D Program of China (grant number 2020YFA0308800), the NSF of China (grant numbers 12074009, 11774009, 62174013, 12061131102 and 11734003), BIT (number 2021CX11013) and the National Key R&D Program of China (2017YFA0206301); the National Research Foundation, Singapore, under its Competitive Research Programme (NRF-CRP22-2019-0007 and NRF-CRP22-2019-0004), under its NRF-ISF joint research programme (NRF2020-NRF-ISF004-3520); and the Ministry of Education, Singapore, under its AcRF Tier 3 Programme 'Geometrical Quantum Materials' (MOE2018-T3-1-002). H.D., and W.G. acknowledge funding from the National Key Basic Research Program of China (2017YFB0701603) and NSFC (number 51971037). We thank X. Dai and H. M. Weng for discussions and their preliminary attempts on ab initio calculations. Y.-C.L. and K.S. acknowledge the JSPS-KAKENHI (JP16H06333 and JP22H05478), (18K14119), the JST-CREST programme (JPMJCR20B1, JMJCR20B5 and JPMJCR1993), the JSPS A3 Foresight Program, and the Kazato Research Encouragement Prize. Y.G. acknowledges funding from the Innovation Program of Shanghai Municipal Education Commission (number 2019-01-07-00-09-E00020), Shanghai Municipal Science and Technology Commission (18JC1412800). Jianhui Zhou was supported by the High Magnetic Field Laboratory of Anhui Province. Yugui Yao acknowledges the Strategic Priority Research Program of Chinese Academy of Sciences (grant number XDB30000000).

Author contributions Jiadong Zhou, W.Z., Y.-C.L. and J.C. contributed equally to this work. W.Z. and X.W. initiated the project and observed the novel Hall effect. Jiadong Zhou and Z.L. proposed the heterodimensional superlattice concept and coordinated the project. Jiadong Zhou and Y.Z. synthesized the superlattice and carried out the Raman and atomic force microscopy measurements. Y.Z. analysed the XPS data. Yuan Yao carried out preliminary STEM experiments. Y.-C.L. and K.S. performed the STEM and EELS measurements. W.Z., B.J. and X.W. carried out the device measurements. Yugui Yao, Y.W. and Y. Hou discussed the structure. Yugui Yao, X.W., Jianhui Zhou, J.C. and Jiadong Zhou discussed the theory calculation process. H.D., W.G. J.C., Jianhui Zhou, W.J. and Yugui Yao performed the theory calculation. J.C., Jianhui Zhou, W.J. and Yugui Yao performed the calculations. X.C. and Y. Huang helped to perform the FIB. J.S. performed the SHG measurements. W.Z. and S.S.P.P. performed the MOKE measurement. B.T., B.L., Q.F. and C.Z. discussed the SHG. All authors contributed to the discussion of the results.

Competing interests The authors declare no competing interests.

Additional information

Supplementary information The online version contains supplementary material available at https://doi.org/10.1038/s41586-022-05031-2.

Correspondence and requests for materials should be addressed to Jiadong Zhou, Yugui Yao, Kazu Suenaga, Xiaosong Wu or Zheng Liu.

Peer review information *Nature* thanks Kai Xiao and the other, anonymous, reviewer(s) for their contribution to the peer review of this work.